Available online at www.sciencedirect.com
ScienceDirect
Computers and Fluids 00 (2018) 1–19
Computers and Fluids

CFD-CSD coupled analysis of underwater propulsion using a biomimetic fin-and-joint system

Howard Chung[a], Shunxiang Cao[a], Michael Philen[a], Philip S. Beran[b], Kevin G. Wang[a,*]

[a]Department of Aerospace and Ocean Engineering, Virginia Polytechnic Institute and State University, Blacksburg, VA 24061, United States
[b]Aerospace Systems Directorate, Air Force Research Laboratory, Wright-Patterson Air Force Base, OH 45433, United States

Abstract

The remarkable performance of various species of fish in propulsion and maneuvering has motivated the design and analysis of flexible, biomimetic underwater propulsors, which may be particularly suitable to small-scale, unmanned vehicles. In this work, we employ a novel fluid-structure coupled computational framework, referred to as FIVER (a FInite Volume method based on Exact Riemann solvers), to simulate the flapping motion of a fin-and-joint system, which mimics the caudal peduncle and caudal fin of fish, and serves as a simplified engineering model of tail-dominated fish propulsion. This problem is dominated by fluid-structure interaction, featuring a three-dimensional, unsteady fluid flow, large structural motion and deformation, and strong added-mass effect. To handle these challenges, we apply an embedded boundary method and a numerically-stable partitioned procedure to couple a hybrid finite volume – finite element computational fluid dynamics (CFD) solver and a nonlinear finite element computational structural dynamics (CSD) solver. First, we validate the CFD and CSD models using experimental data in fundamental vibration frequency, hydrodynamic forces, and structural displacement. Next, we investigate the fluid and structural dynamics, as well as the propulsive performance, focusing on the two-way fluid-structure coupling and the three-dimensional flow variation, which supplements the existing body of literature on biological and bio-inspired fluid dynamics. Further, by comparing a wide, trapezoidal fin and a narrow, forked fin, we investigate the various effects of fin geometry, and more generally, also demonstrate the use of observations and knowledge of biological diversity in the design of engineering systems.

Keywords: fluid-structure interaction, CFD-CSD coupled simulation, biomimicry, unconventional propulsor, experimental validation

1. Introduction

Autonomous and remotely operated underwater vehicles have been envisioned to augment and replace manned platforms and fixed systems in a wide variety of science, commercial, and military missions such as collecting oceanographic data [1], inspecting undersea infrastructure [2], monitoring fish farms [3], and sweeping mines [4]. In many cases, these vehicles need to be versatile, capable of performing multiple tasks with different locomotion gaits. For example, an ocean sampling robot should be able to swim efficiently to achieve long endurance and hold position under strong ocean waves. A pipeline inspection vehicle needs to be able to cruise efficiently and navigate in complex environments. These versatility requirements are often beyond the capability of conventional propulsors, such as marine propellers and underwater gliders [5].

Meanwhile, the ability of fish to swim efficiently at various speeds, accelerate and brake rapidly, maneuver in tight places, and hover in an unsteady flow has motivated the design and analysis of unconventional, flexible propulsors

*Corresponding author
Email address: kevinwgy@vt.edu (Kevin G. Wang)

mimicking the fins and body of fish [6, 7, 8]. In this regard, various studies have revealed the necessity of designing and modulating the propulsor's geometry and material properties (e.g., elasticity and viscoelasticity properties), in order to achieve the desired locomotion goal [9, 10, 11]. Nonetheless, the dynamic interaction between flexible propulsors and the surrounding fluid medium, and the effect of this two-way coupling on propulsive performance, is still an open research area.

The present study aims to investigate the fluid and structural dynamics of a biomimetic fin-and-joint system, which serves as a simplified engineering model of tail-dominated fish propulsion (e.g., subcarangiform, carangiform, thunniform, ostraciiform [12]). The system consists of two flexible plates of different shapes and dimensions, referred to as the *fin* and the *joint*, which mimick, respectively, the caudal fin and caudal peduncle of fish (Figure 1). Recently, Kancharala and Philen [13, 14] fabricated specimens of this configuration using polycarbonate (PC) sheets, with fin thickness varying from 0.2 to 3.2 mm. They conducted water tunnel experiments where the specimens undergo prescribed periodic flapping motion, and measured the time-histories of hydrodynamic forces and structural deformation. Nonetheless, the three-dimensional (3D), unsteady fluid dynamics is still unclear. The authors developed a simplified numerical model that couples a two-dimensional (2D) unsteady panel method with structural deformation measured using digital image correlation (DIC). The model is able to capture the qualitative trend of lower thrust force as fin stiffness was increased. However, it does not accurately predict the magnitude of hydrodynamic forces [13], which indicates the need of a higher-fidelity numerical model to properly simulate the fluid flow.

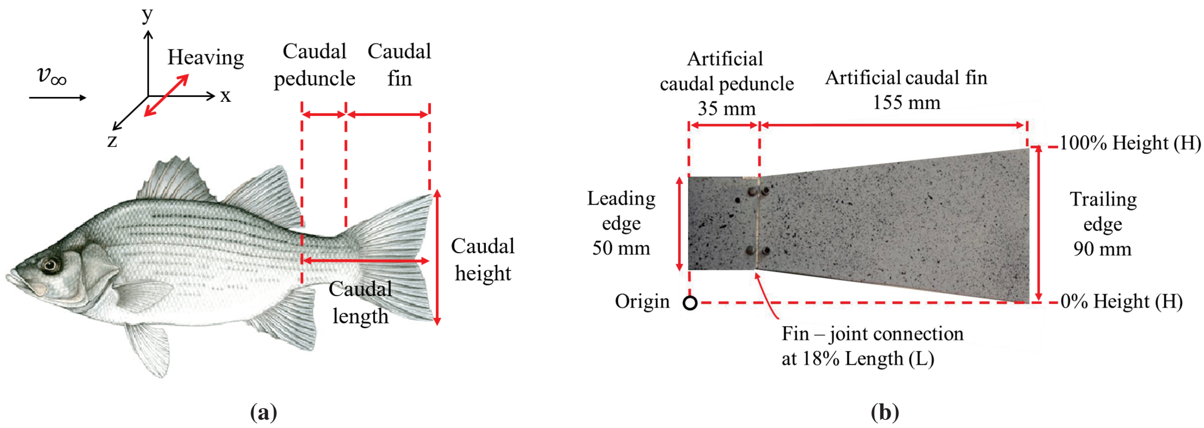

Fig. 1. A biomimetic fin-and-joint system: The caudal peduncle and fin of a white bass (*Morone chrysops*) (a) and a simplified engineering model (b).

In this work, we start with developing and validating a computational fluid dynamics (CFD) - computational structural dynamics (CSD) coupled simulation model basing on the experiments of Kancharala and Philen mentioned above. Then, we analyze the variation and evolution of the 3D, unsteady fluid flow in space — both chordwise and spanwise — and in time. Further, we modify the simulation model to obtain a "forked" fin and, by comparison with the original model, investigate the effects of fin geometry on the coupled fluid and structural dynamics, and the propulsive performance. The computational framework employed in this study couples a CFD solver and a CSD solver using a "W-shape" partitioned procedure [15, 16, 17]. The CFD solver solves the viscous, compressible Navier-Stokes equations using a hybrid finite volume – finite element method. It is equipped with a low-Mach preconditioner [18] and an implicit time-integrator to efficiently simulate low-speed flows in a relatively large time window (5 to 10 s). The flow is assumed to be laminar. This assumption can be justified by 2D and 3D digital particle image velocimetry (DPIV) measurements obtained from fin propulsion experiments at similar scales (e.g., [9, 11]). The finite element CSD solver uses the nonlinear ANDES shell element [19] to handle large structural deformation. The large deformation of the propulsor also requires robust and accurate numerical methods to track the time-dependent fluid wall boundary, and — in the context of partitioned procedures — to transfer fluid-induced loads to the structure. A recently developed embedded boundary method [16, 20] is employed to address these issues. This computational methodology has been verified and validated in the past for several science and engineering applications, including micro air vehicles (MAVs) with flexible flapping wings mimicking those of birds and bats [17, 21, 22]. Nonetheless, its application to hydroelasticity and underwater propulsion is a novelty of the present paper.

Within the past decade, non-body-conforming CFD techniques, such as embedded boundary, immersed boundary [23], and fictitious domain [24] methods, have been applied to simulate biological and bio-inspired fluid flows involving large boundary deformation (e.g., [25, 26, 27, 28]). In most of these studies, the fluid and the propulsor are "one-way" coupled in the sense that the motion of the propulsor is prescribed using either an analytical function or data from experimental measurement. This approach has been shown to be effective for capturing flow information and conducting parameter studies, which are often difficult to accomplish in laboratory experiments. On the other hand, two-way, CFD-CSD coupled analysis that predicts both the fluid dynamics and the propulsor deformation is scarce in the literature. This type of multiphysics analysis, as explored in the present study, may potentially improve researchers' understanding of the causal relationship of the propulsor forces, the propulsor kinematics, and the hydrodynamics.

The remainder of this paper is organized as follows. Section 2 summarizes the physical models and numerical methods in the 3D CFD-CSD coupled computational framework. Section 3 validates the CFD model through one-way coupled simulations in which the structural motion and deformation are prescribed using the digital image correlation (DIC) measurements obtained from experiment. Section 4 presents the development and validation of a nonlinear finite element model of the fin-and-joint system. Section 5 presents several two-way coupled simulations, and investigates the coupled fluid and structural dynamics, as well as the effect of fin geometry. Finally, concluding remarks are provided in Section 6.

2. Computational framework

We employ a recently developed CFD-CSD coupled computational framework, referred to as "FIVER" (a FInite Volume method based on Exact Riemann solvers) [15, 16, 29, 17, 20], to simulate the dynamic fluid-structure interaction associated with the biomimetic fin-and-joint system, which involves a 3D unsteady fluid flow, large structural deformation, and strong added mass effect.

Let $\Omega_F \subset \mathbb{R}^3$ denote the fluid domain of interest. The CFD solver solves the 3D Navier-Stokes equations governing viscous, compressible flow, which can be written as

$$\frac{\partial \mathbf{W}}{\partial t} + \nabla \cdot \mathbf{F}(\mathbf{W}) = \nabla \cdot \mathbf{G}(\mathbf{W}), \qquad \text{in } \Omega_F, \tag{1}$$

where

$$\mathbf{W} = \begin{bmatrix} \rho \\ \rho\mathbf{v} \end{bmatrix}, \qquad \mathbf{F} = \begin{bmatrix} \rho\mathbf{v} \\ \rho\mathbf{v} \otimes \mathbf{v} + p\mathbf{I} \end{bmatrix}, \qquad \mathbf{G} = \begin{bmatrix} 0 \\ \mathbf{T} \end{bmatrix}. \tag{2}$$

ρ, $\mathbf{v}$, p denote the density, the velocity vector, and the pressure of the flow, respectively. $\mathbf{T}$ denotes the viscous stress tensor, given by

$$\mathbf{T} = \mu\left(\nabla\mathbf{v} + (\nabla\mathbf{v})^T - \frac{2}{3}(\nabla \cdot \mathbf{v})\,\mathbf{I}\right), \tag{3}$$

where $\mu = 1.0 \times 10^{-3}$ Pa·s is the dynamic viscosity of liquid water at 20 °C. $\mathbf{I}$ denotes the 3×3 identity matrix. Tait's barotropic equation of state (EOS) is applied to model liquid water, which closes the above system of equations. Specifically, the EOS can be written as

$$p = p_0 + \alpha\left(\left(\frac{\rho}{\rho_0}\right)^{\beta} - 1\right), \tag{4}$$

where $\alpha = 290$ MPa, $\beta = 7.15$ are experimentally calibrated model parameters for liquid water [30]. The reference density (ρ_0) and pressure (p_0) are set by $\rho_0 = 1.0 \times 10^3$ kg/m^3 and $p_0 = 1.0 \times 10^5$ Pa, respectively. The governing equation Eq. (1) is semi-discretized on unstructured tetrahedral mesh using a hybrid finite volume-finite element method. Specifically, the convective fluxes, $\mathbf{F}(\mathbf{W})$, are computed using a finite volume method with Roe's approximate Riemann solver and the MUSCL (monotonic upwind scheme conservation law) scheme. The viscous fluxes, $\mathbf{G}(\mathbf{W})$, are computed using the P1 finite element approximation, leading to constant viscous stress within each tetrahedral element. In this work, the fluid velocity of interest is of the order of 0.1 to 1.0 m/s. To overcome the numerical difficulties (e.g., spurious solution oscillations and slow convergence) plaguing finite volume compressible flow solvers in the low Mach regime, Turkel's low-Mach preconditioner [18] is applied to the Roe flux function. The system of ordinary differential equations resulting from semi-discretization can be expressed in a compact form as

$$\frac{d\mathbf{W}_h}{dt} + \widetilde{\mathbf{F}}(\mathbf{W}_h) = \widetilde{\mathbf{G}}(\mathbf{W}_h), \tag{5}$$

where $\mathbf{W}_h$, $\widetilde{\mathbf{F}}$ and $\widetilde{\mathbf{G}}$ denote the cell-averaged fluid state and the numerical flux functions over the entire mesh.

Let $\Omega_S(t) \subset \mathbb{R}^3$ denote the structural domain at time t. Hence $\Omega_S(0)$ denotes the initial configuration of the fin-and-joint system. The CSD solver solves the equation of dynamic equilibrium, which can be written in the Lagrangian setting as

$$\rho^S \frac{\partial^2 u_j}{\partial t^2} = \frac{\partial}{\partial x_i}\left(\sigma_{ij} + \sigma_{im}\frac{\partial u_j}{\partial x_m}\right) + b_j, \qquad \text{in } \Omega_S(0), \qquad j = 1, 2, 3, \tag{6}$$

where the subscripts i, j, m varying between 1 and 3 designate the spatial coordinate system. ρ^S denotes the structural material density, $\mathbf{u}$ the displacement vector field, $\boldsymbol{\sigma}$ the second Piola-Kirchhoff stress tensor, and $\mathbf{b}$ the vector of body forces. Eq. (6) is semi-discretized by the Galerkin finite element method, which yields

$$\mathbf{M}\frac{\partial^2 \mathbf{U}_h}{\partial t^2} + \mathbf{f}^{int}(\mathbf{U}_h) = \mathbf{f}^F(\mathbf{W}_h) + \mathbf{f}^{ext}, \tag{7}$$

where $\mathbf{M}$ denotes the mass matrix, $\mathbf{U}_h$ denotes the vector of discrete structural displacement. $\mathbf{f}^{int}$, $\mathbf{f}^F$ and $\mathbf{f}^{ext}$ are the vectors of internal forces, flow-induced forces on wet surface of structure and other external forces, respectively.

The interaction between the fluid and structure subsystems is governed by two transmission conditions at the fluid-structure interface $\Gamma^{FS} = \partial\Omega_F \cap \partial\Omega_S$, namely the kinematic, non-penetration condition

$$v_i - \frac{\partial u_i}{\partial t} = 0, \qquad \text{on } \Gamma^{FS}, \qquad i = 1, 2, 3, \tag{8}$$

and the equilibrium condition

$$\left(\frac{1}{J}\left(\sigma_{km} + \sigma_{kj}\frac{\partial u_m}{\partial x_j}\right)\left(\frac{\partial u_i}{\partial x_m} + \delta_{im}\right) - T_{ki} + p\delta_{ki}\right)\cdot n_k^{FS} = 0, \qquad \text{on } \Gamma^{FS}, \qquad i = 1, 2, 3, \tag{9}$$

where the Einstein summation convention is used for notational brevity. $J = \det(\frac{\partial u_i}{\partial x_m} + \delta_{im})$, $\mathbf{n}^{FS}$ denotes the unit normal to the deformed configuration of Γ^{FS}, and δ denotes the Kronecker delta function. These two transmission conditions are imposed to the semi-discretized fluid and structural governing equations (Eqs. (5) and (7)) using a second-order accurate partitioned procedure [15] and an embedded boundary method [16, 21] (Figure 2). Specifically, the temporal discretization of Eqs. (5) and (7) are off-set by half a time step, as shown in Figure 2(b). At each time step, the CSD solver sends the structural displacement and velocity on Γ^{FS} to the CFD solver. The CFD solver operates on a fixed CFD mesh, despite the motion of the fluid-structure interface (Figure 2(a)). The location of the interface is tracked on the CFD mesh using a collision-based computational geometry algorithm [20]. The non-penetration condition (Eq. (8)) is enforced by solving one-dimensional fluid-structure Riemann problems (hence the name "FIVER"). Then, the CFD solver advances for one time-step, and sends the fluid-induced loads to the CSD solver, thereby enforcing the equilibrium condition. The embedded boundary method used in this work introduces a first-order geometric error at the fluid-structure interface. In general, achieving second-order convergence rate in 3D, realistic problems using embedded and immersed boundary methods is still challenging. A recent effort has extended FIVER to second-order accuracy, but only for inviscid flows [31].

Both the CFD and the CSD solvers are parallelized using the message passing interface (MPI). The simulations presented in this paper each consumes approximately 3,000 to 6,000 CPU hours on the BlueRidge computer cluster at Virginia Tech [32].

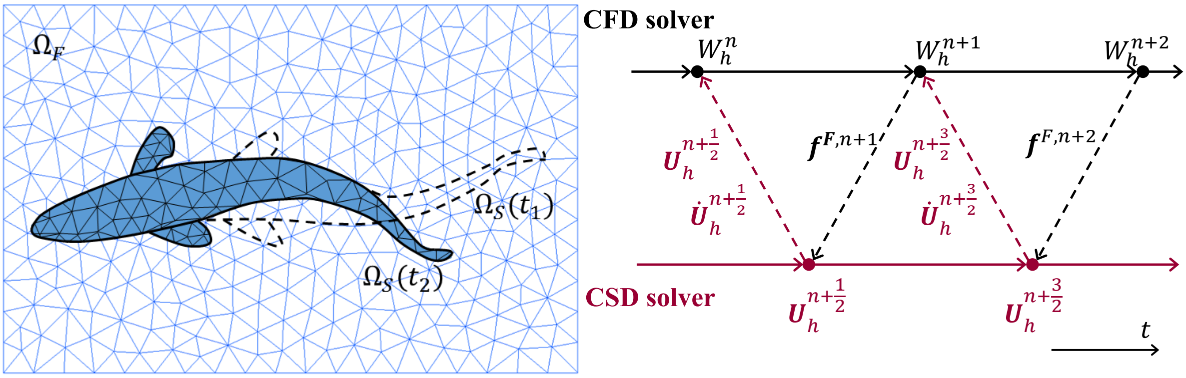

(a) **(b)**

Fig. 2. Illustration of the embedded boundary method for enforcing the fluid-structure transmission conditions (a) and a "W-shape" partitioned procedure for coupling the CFD and CSD solvers (b).

3. CFD-DIC coupled analysis

As a first step, we simulate the water tunnel experiment conducted by Kancharala and Philen (summarized in Appendix A) by coupling the 3D, embedded boundary CFD solver presented in Section 2 with the digital image correlation (DIC) measurement of the structural motion and deformation. The objective is to validate the CFD model, and to compare with the simplified numerical model presented in [13], which assumes a 2D potential flow and employs a vortex panel method.

A 3D fluid domain, $\Omega_F = \{(x, y, z) \in \mathbb{R}^3 \,\big|\, -325 \text{ mm} < x < 325 \text{ mm}, -76.2 \text{ mm} < y < 76.2 \text{ mm}, -76.2 \text{ mm} < z < 76.2 \text{ mm}\}$, is defined, following the dimensions of the test section of the water tunnel used in the experiment (Figure 3). Ω_F is discretized by an unstructured tetrahedral mesh with approximately 1.5 million nodes and 9 million tetrahedral elements. The most refined region of the mesh, that is, the region traversed by the structural specimen, has a characteristic element size of 0.95 mm (Figure 4). The no-slip boundary condition, i.e. $v = 0$ m/s, is imposed on the wall boundaries of the fluid mesh. The freestream velocity $v_\infty = 0.1$ m/s is specified at the inlet boundary. In order to assess the effect of fin thickness on the hydrodynamic forces, six simulations are performed in which the fin thickness τ is set to 0.2 mm, 0.4 mm, 0.7 mm, 1.2 mm, 1.6 mm and 3.2 mm, respectively. In all the simulations, the fin-and-joint system (i.e. the propulsor) is discretized by a surface mesh with 4,186 nodes and 8,100 triangle elements (Figure 4). The motion and deformation of this discretized surface is prescribed using the DIC measurement obtained from experiment. Unlike the vortex panel-DIC coupled analysis presented in [13], in which only the measurement of centerline displacement is used (180 sample points), the complete 3D structural deformation obtained through DIC is used in the CFD-DIC coupled simulations. Specifically, the 3D displacement at 16,000 sample points over the specimen is collected using DIC at a frequency of 12 Hz. At each time step, the nodal displacement of the surface mesh is prescribed by linearly interpolating the DIC measurement both in space and in time. In all the simulations, a constant time-step of $\Delta t = 0.002$ s is applied, and the simulation is terminated at $t = 2$ s when the propulsor has completed 2.6 cycles of flapping motion.

Figure 5 presents the time-averaged thrust predicted by the CFD-DIC coupled simulations, in comparison with the corresponding experimental data and results of the vortex panel–DIC coupled simulations. Overall, the result from CFD–DIC coupled simulations is in good agreement with the experimental data. In particular, it captures the trend that thinner, hence more flexible, fins generate higher thrust force. It is also significantly more accurate — that is, by 1 to 2 orders of magnitude — than the result from the vortex panel–DIC coupled simulations. The remaining discrepancy between the CFD–DIC coupled simulations and the experiment may be related to the fact that some secondary components of the specimen (e.g., a rod clamping the leading edge of the fin) are not modeled. Another possible source of error is the relatively low sampling frequency of the DIC and the linear interpolation applied to obtain a higher temporal resolution.

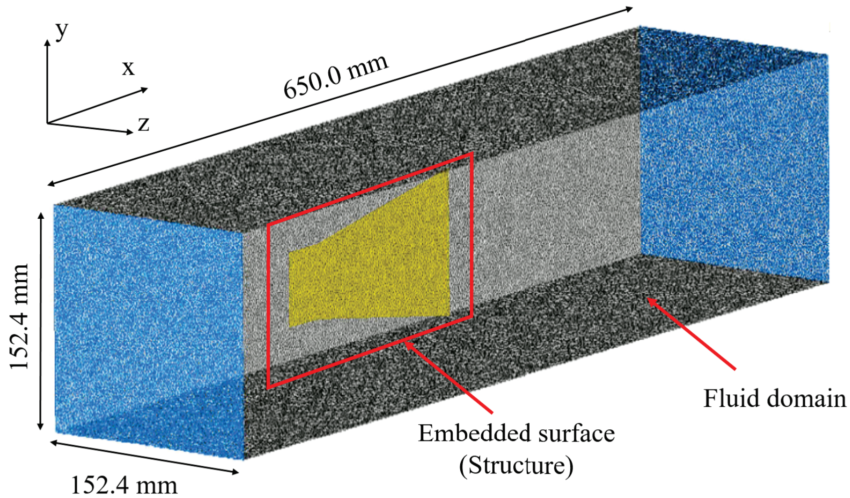

Fig. 3. Simulation setup.

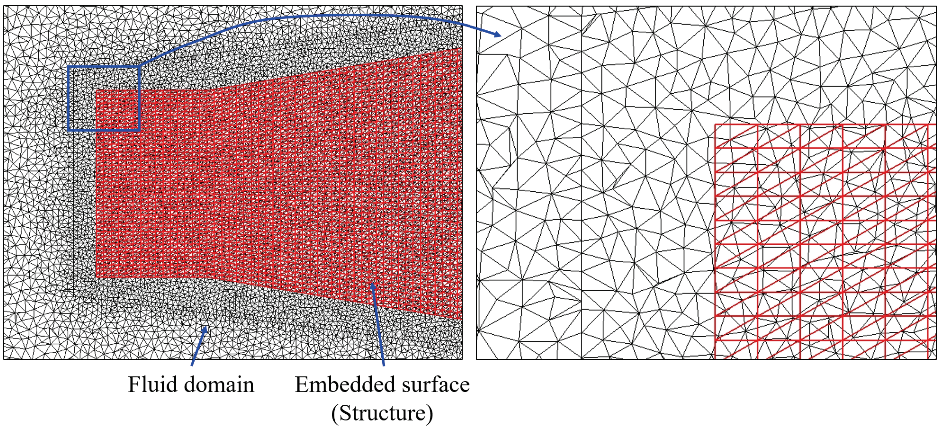

Fig. 4. Local refinement of the CFD mesh.

4. A nonlinear finite element model of the fin-and-joint system

We develop and validate a finite element model of the fin-and-joint system. Given the small thickness-to-length ratio (0.001 $\sim$ 0.02) and the large deformation, the nonlinear ANDES shell element proposed in [19] is used to represent both the fin and the joint. The ANDES formulation is based on an extended parameterized variational principle, where only the deviatoric part of the strains is assumed over the element, whereas the mean strain part is discarded in favor of a constant stress assumption [19]. Here, the joint is discretized using 336 nodes and 300 quadrangle elements, while the fin is discretized using $1,986$ nodes and $1,900$ elements (Figure 6). The fin and joint are connected by 21 shared nodes at $18\%L$. The characteristic element size is approximately 2 mm. The density, Young's modulus, and Poisson's ratio of the polycarbonate material are shown in Table 1.

Following the experiment setup, a heaving motion with frequency $f = 1.3$ Hz and amplitude of $A = 20$ mm is prescribed to the nodes on the leading edge of the propulsor, using the following sinusoidal displacement and velocity

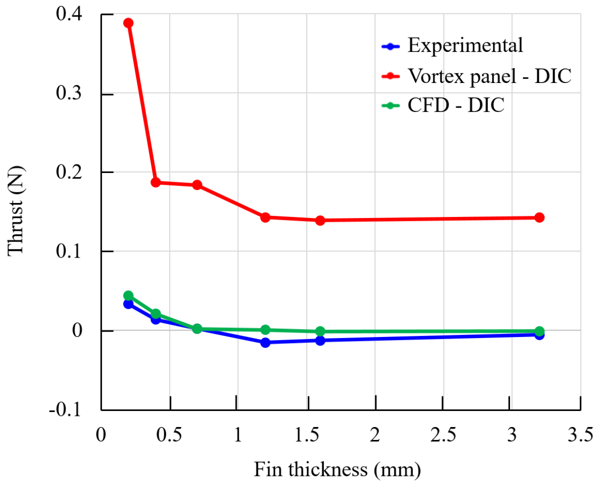

Fig. 5. Time-averaged thrust generation by propulsors with various fin thickness.

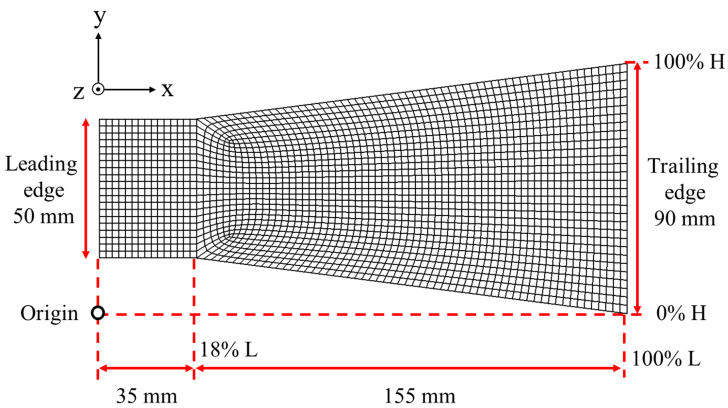

Fig. 6. The CSD model of the fin-and-joint system.

Parameter	Value
Young's Modulus, E (GPa)	2.1
Poisson's Ratio, ν_s	0.3
Density, ρ (kg/m^3)	1040

Table 1: Material properties of Polycarbonate used in simulations.

functions:

$$z(t) = A\cos(\omega t) - A, \tag{10}$$
$$\dot{z}(t) = -A\omega\sin(\omega t), \tag{11}$$

where $\omega = 2\pi f$. The propulsor is initially placed on the x-y plane with $z = 20$ mm. Using the heaving motion prescribed above, the initial displacement $z(0)$ and initial velocity $\dot{z}(0)$ are both zero. This ensures that the initial condition of the structure is consistent with that of the fluid flow obtained from a steady-state CFD simulation.

We have conducted "dry" simulations to verify mesh convergence, in which the CSD solver is decoupled from the CFD solver, hence the structural model does not receive hydrodynamic load. It is found that refining the mesh described above by a factor of 2 gives only 3% difference in the trailing edge displacement.

Further, to validate the CSD model, we conduct numerical modal analysis and laboratory modal testing side by side. In the modal testing, the structural specimen is cantilevered at the leading edge, and excited with an electro-magnetic shaker. A National Instruments system with a PXI-4461 (24-Bit, 204.8 kS/s, 2-input/2-output) is used to simultaneously excite the cantilever fin and measure the trailing edge velocity. A Polytec laser vibrometer is used to measure the trailing edge velocity. The fundamental frequency obtained by modal testing is then compared with that obtained from modal analysis (Figure 7). It can be observed that the fundamental frequency obtained by both modal testing and modal analysis are in good agreement. The discrepancy (between 0.38% and 8.69%) could be due to the imperfection in enforcing a fixed-free boundary condition in experiments. Another possible source of error is the non-uniformity in material properties in the artificial fin-and-joint specimens, which is not accounted for in the numerical analysis.

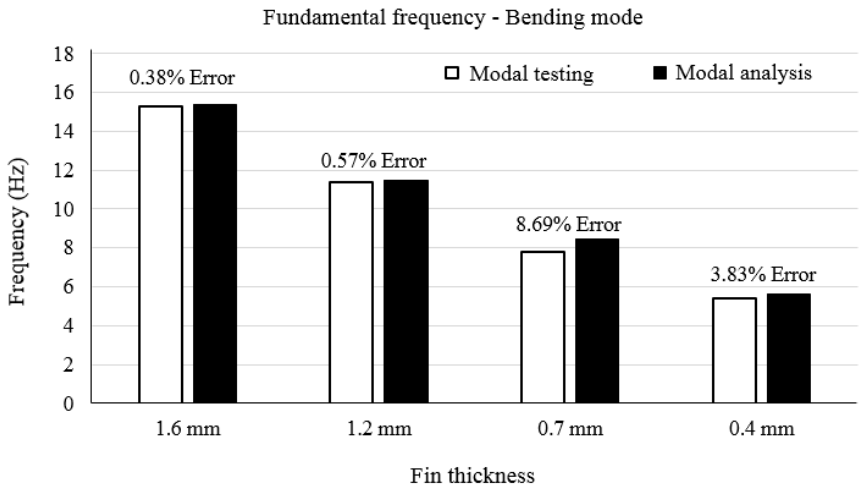

Fig. 7. Validation of the CSD model for the fundamental frequency of the fins.

5. CFD-CSD coupled analysis

After validating the CFD and CSD models, we conduct two-way, fluid-structure coupled simulations using the partitioned procedure and embedded boundary method described in Section 2. The same CFD and CSD domains and meshes presented in Sections 3 and 4 are used. The semi-discretized fluid and structural governing equations are integrated using the second-order accurate fluid-structure time-integrator presented in Section 2. Specifically, the implicit three-point backward difference is used in the CFD solver while the implicit Newmark time integrator with $\beta = 0.3$ and $\gamma = 0.6$ [33] is used in the CSD solver. A constant time step of $\Delta t = 8.0 \times 10^{-4}$ s is used for both solvers.

5.1. Structural motion and deformation

Figure 8 shows the structural motion and deformation predicted by the CFD-CSD coupled simulation, in comparison with results from the water tunnel experiment and a "dry" simulation, that is, a dynamic CSD simulation without imposing the hydrodynamic load. The propulsor with fin thickness $\tau = 1.6$ mm is used here as example. Evidently, the effect of the hydrodynamic load, and essentially the fluid-structure interaction, is significant. The maximum lateral displacement (i.e. displacement in z-direction) at the trailing edge decreases from approximately 40 mm in the dry simulation to approximately 15 mm in the CFD-CSD coupled simulation. Notably, the hydrodynamic load leads to a "phase lag" along the length of the propulsor. Most of the time, the leading and trailing edges of the structure move in opposite directions, with a virtual pivot at approximately $2/3$ of the length from the leading edge, which undergoes minimum displacement. We also note that the result of the CFD-CSD coupled simulation agrees reasonably well with the DIC measurement from the experiment. The overall motion and deformation pattern is accurately captured. The location of minimum lateral displacement (i.e. the virtual pivot) differs by 10.1%. The discrepancies are likely due to the fact that some small components of the specimen used in experiment — specifically, a thin aluminum strip and four nuts and bolts — are not modeled. These components are not designed for performance purpose, but rather as a method to connect the fin and the joint. Therefore, they are not modeled in the simulations.

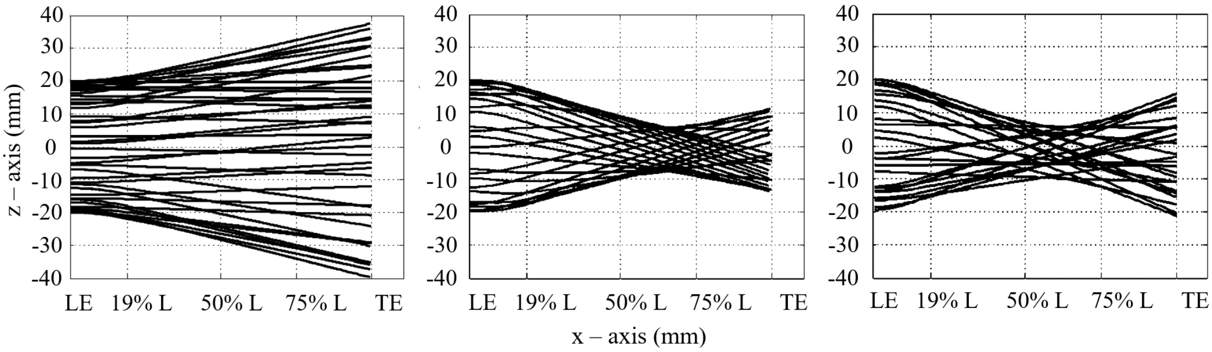

(a) Dry simulation **(b)** CFD-CSD coupled simulation **(c)** Experiment

Fig. 8. Midline (i.e. the line connecting the middle points of the leading edge (LE) and trailing edge (TE)) displacement obtained by (a) a dry simulation, (b) the two-way coupled Simulation, and (c) digital image correlation (DIC) in a water tunnel experiment. In each sub-figure, 25 - 35 snapshots taken with a frequency of 12.5 Hz for (a) - (b), and 12 Hz for (c), are superposed.

5.2. Vortex-dominated fluid dynamics

5.2.1. Vortex generation

Figure 9 presents vorticity isosurfaces at time $t = 0.09$ s, when the leading edge of the propulsor just starts moving in the negative z-direction. Specifically, Figure 9(a) displays the isosurface of fixed vorticity magnitude, $|\zeta| = 10\ \mathrm{s}^{-1}$, while Figures 9(b), 9(c), and 9(d) show the isosurfaces of the x-, y-, and z-component of vorticity at $\zeta = \pm 10\ \mathrm{s}^{-1}$. The red and blue arrows in the figures indicate the directions of the vortices. As expected, vortices are generated on the surface, the leading edge, the trailing edge, as well as the upper and lower edges of the propulsor.

In particular, Figure 9(b) shows that as the leading edge of the propulsor moves in the negative z-direction under prescribed motion, the pressure differential on the two sides of the propulsor generates vortices at the upper and lower edges. Walking from the leading edge downstream, it is notable that the direction of these vortices changes at approximately $2/3$ of the length. This can be explained by the fact that the leading and trailing edges move in opposite directions, which results from the elasticity of the structure and the strong added mass effect of the heavy fluid. This finding may further indicate that when the elastic properties of a fin propulsor are carefully designed, complex propulsor kinematics — such as flapping or undulation — and vortex dynamics may be achieved by actuating only a small region of the propulsor, e.g., the leading edge.

5.2.2. Wake flow and thrust generation

For ease of comprehension, we introduce a nondimensional time t^*, by normalizing time t by the period of the prescribed motion $T_p = 0.77$ s, i.e.

$$t^* = \frac{t}{T_p}. \tag{12}$$

Vortex rings. Figure 10 shows a side view (i.e. x-y plane) of vorticity isosurfaces at $t^* = 2.5$. At this time, the propulsor has completed 2.5 cycles of flapping motion, therefore the wake vortices can be clearly observed. The values of vorticity isosurfaces are the same as those in Figure 9, i.e. $|\zeta| = 10\ \mathrm{s}^{-1}$ for Figure 10(a), and $\zeta = \pm 10\ \mathrm{s}^{-1}$ for 10(b), 10(c), and 10(d). The opacity of the isosurfaces is reduced to 50% to assist visualization in the z-direction.

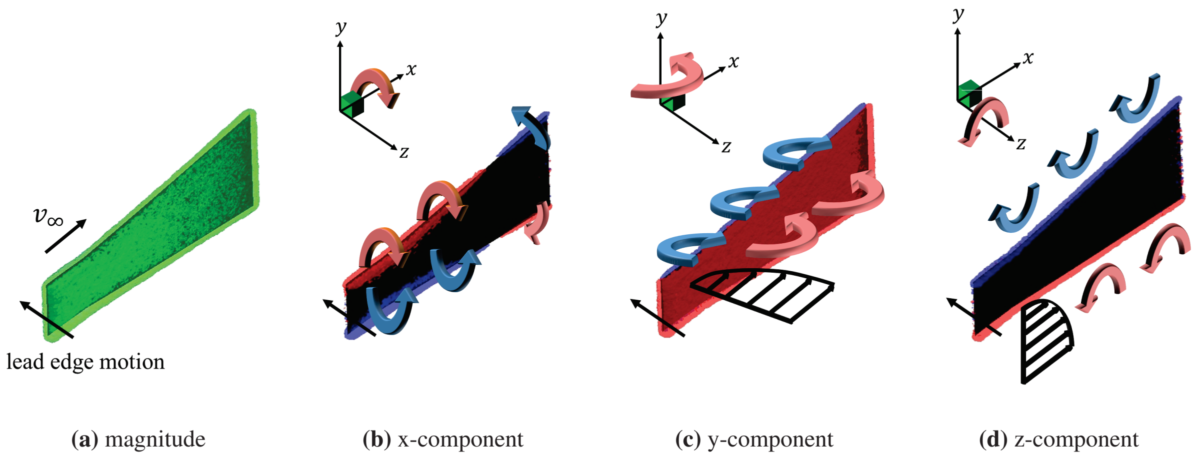

Fig. 9. 3D perspective vorticity isosurfaces at t = 0.09 s. (a): the isosurface of fixed magnitude, $|\zeta| = 10\ s^{-1}$; (b): the x-component, $\zeta = \pm 10\ s^{-1}$; (c) the y-component, $\zeta = \pm 10\ s^{-1}$; and (d): the z-component, $\zeta = \pm 10\ s^{-1}$. Red: counterclockwise rotating vortices. Blue: clockwise rotating vortices.

192 Figures 10(a) and 10(c) show a chain of linked vortex rings with alternating signs in the wake of the propulsor, which
193 is consistent with observations in many biological and biomimetic fin propulsion experiments (e.g., [34, 35]).

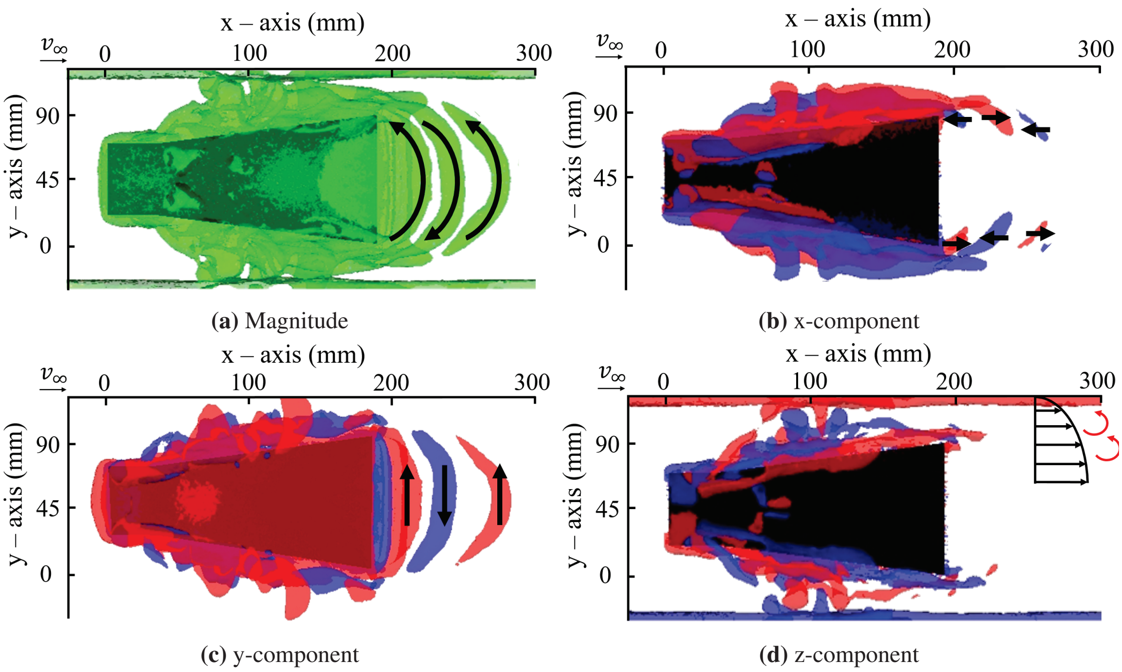

Fig. 10. Side view ($x - y$ plane) of vorticity isosurfaces at $t^* = 2.5$ (i.e. $t = 1.92$ s). (a): The isosurface of fixed magnitude, $|\zeta| = 10\ s^{-1}$; (b): the x-component, $\zeta = \pm 10\ s^{-1}$; (c) the y-component, $\zeta = \pm 10\ s^{-1}$; and (d): the z-component, $\zeta = \pm 10\ s^{-1}$. Red: counterclockwise rotating vortices. Blue: clockwise rotating vortices.

194 *Widthwise flow variation: thrust production versus drag production.* The time-averaged total hydrodynamic thrust
195 predicted by the CFD-CSD coupled simulations is in close agreement with the result of CFD-DIC coupled simulations
196 shown in Figure 5. Here, we focus on investigating the variation of the fluid flow and the hydrodynamic force along
197 y-direction, i.e. the direction of propulsor width. This aspect has rarely been discussed in the literature of biological

and bio-inspired fluid dynamics, largely due to challenges in measuring and simulating fluid-structure interactions in 3D.

In this regard, Figure 11 presents the instantaneous vorticity field at $t^* = 9.32$, or $t = 7.17$ s. Specifically, two 2D x-z planes intersecting two width locations — 50%H (mid-width) and 95%H (close to the edge of the propulsor) — are visualized. The wake behind the propulsor, which comprises of an array of trailing discrete vortices with alternating signs, shows the 3D effects of a propulsor with finite width. For the 2D plane at 50%H, the flow between each pair of vortices has a component of velocity oriented downstream (indicated by the yellow arrows), increasing the momentum of the incident flow (Figure 11(a)). This is known in general fluid mechanics as a *reverse von Kármán street*, and is indicative of thrust production [36]. However, for the 2D plane at 95%H, the wake flow is dramatically different: it consists of staggered counter-rotating vortices with flow oriented upstream, decreasing the momentum of the incident flow (Figure 11(b)). This is known as the *von Kármán street*, and is indicative of drag production.

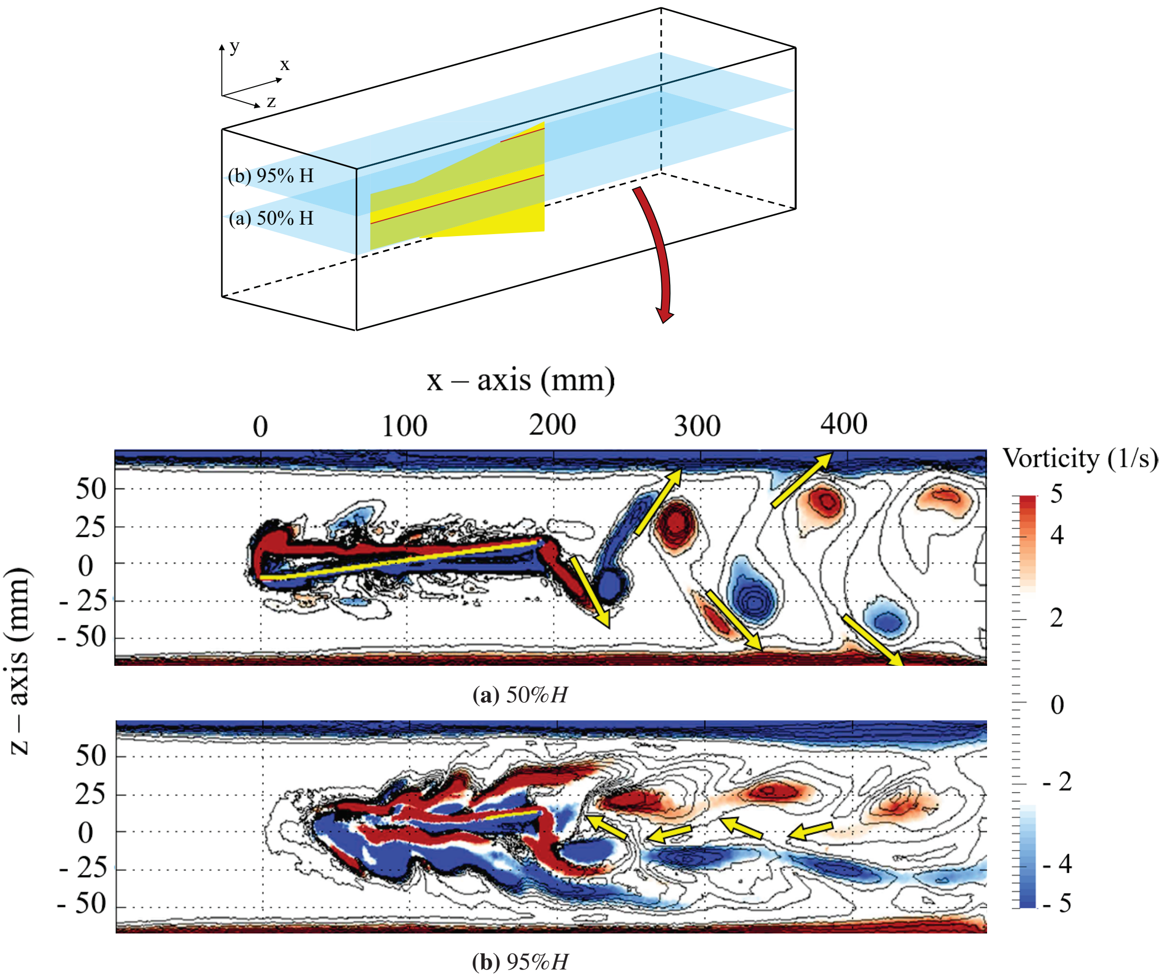

Fig. 11. The instantaneous vorticity field at $t^* = 9.32$, visualized on two x-z cross-sections intersecting, respectively, the midline (50%H) and edge (95%H) of the propulsor. Red: counterclockwise rotating vortices. Blue: clockwise rotating vortices.

Further, we compute and visualize the time-averaged flow velocity on the same two x-z planes (Figure 12). In addition, the velocity along z-axis at $x = 232$ mm, which is 22%L aft of the trailing edge, is plotted separately for a closer inspection (Figures 12(c) and 12(d)). Again, results on the two cut planes differ significantly. A jet flow directed downstream is observed on the 50%H plane (Figure 12(a)). In the wake, the 1D plot clearly shows a momentum surfeit wake, i.e. $v/v_\infty > 1.0$ (Figure 12(c)). This suggests a thrust production region in the propulsor. On the other hand, for the 95%H plane, a jet that redirects flow back upstream is observed (Figure 12(b)). Also, a momentum deficit wake is evident by inspecting the 1D plot (Figure 12(d)). This suggests a drag production region in the propulsor.

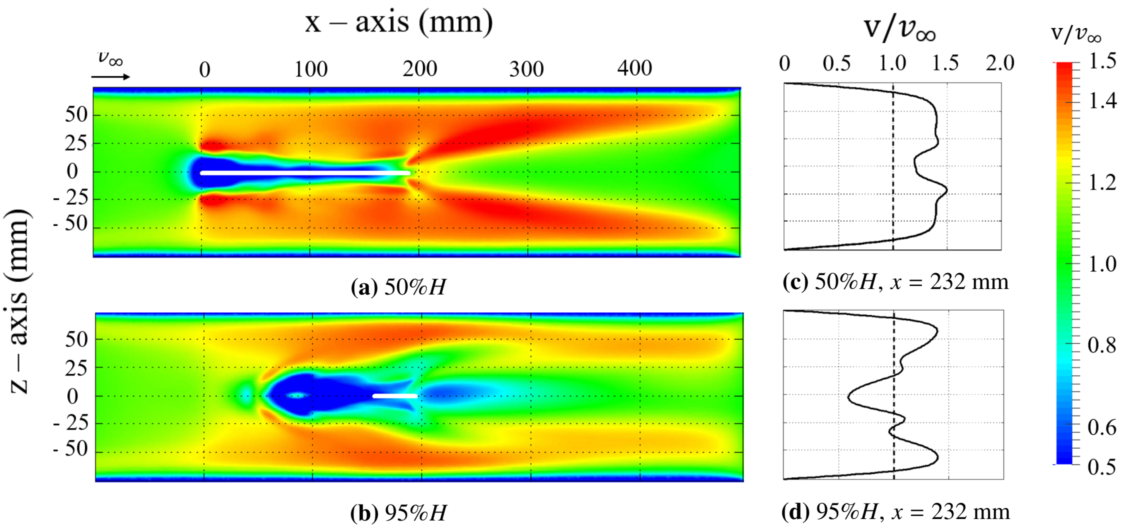

Fig. 12. Time-averaged velocity field on two x-z cross-sectons intersecting (a) 50%H and (b) 95%H, and along the line at x = 232 mm (i.e. 22%L aft of the trailing edge)

In summary, both the instantaneous flow vorticity and the time-averaged flow velocity exhibit significant variation along the propulsor width. Both fields suggest that, under the simulated conditions, the region around the midline of the propulsion produces thrust, whereas the regions near the upper and lower edges produce drag. More generally, this finding indicates the possibility of rationally designing the shape of a flexible propulsor to improve its thrust production.

5.2.3. Leading and trailing edge vortices

Both the leading edge and the trailing edge of the propulsor shed vortices as they move in the vertical z-direction. These vortices are referred to as leading edge vortices (LEVs) and trailing edge vortices (TEVs), following the literature of biological and bio-inspired fluid dynamics. Given that the propulsor moves forward with respect to the ambient flow (i.e. $v_\infty > 0$), the LEVs are convected downstream, and they inevitably interact with the TEVs. To investigate the interaction, we look at a series of 2D flow snapshots taken on the middle plane (i.e. 50%H), for $4.0 < t^* < 5.0$ (Figure 13). This time interval is the fifth flapping cycle of the propulsor, therefore periodic flow and structural motion have been achieved, and the formation of LEVs and TEVs can be clearly seen. In the figure, the subscript n in LEV$_n$ and TEV$_n$ refers to the LEV and TEV formed during the n^{th} cycle. At $t^* = 4.0$ (Figure 13(a)), the LEVs from cycles $n = 2$ and $n = 4$ can be observed. Both LEVs are carried downstream by the freestream flow at velocity $v_\infty = 0.1$ m/s. Figures 13 (a) and (b) show that as LEV$_2$ travels downstream, its velocity magnitude increases. As it approaches the trailing edge, TEV$_5$ begins to form, and starts to interact with LEV$_2$ (Figures 13 (c) and (d)). This occurs around the time when the leading edge has zero velocity and maximum acceleration. It is also noteworthy that because the ambient flow velocity is small compared to the lateral velocity of the propulsor, the interaction of LEV and TEV is found to occur 3 cycles apart from each other. Comparing Figures 13 (d), (e), and (f), it is interesting to notice that the interaction of LEV$_2$ and TEV$_5$ seems to result in the former disappearing, and the latter gaining velocity and being shed into the wake. Lastly, we note that the snapshot taken at $t^* = 4.00$ (Figure 13 (a)) looks nearly identical to the one taken at $t^* = 5.00$ (Figure 13 (f)), indicating that an unsteady, yet periodic fluid-structure interaction is achieved.

5.2.4. Lateral hydrodynamic force

Figure 14(a) presents the time-history of the total lateral force (i.e. force in z-direction) exerted by the fluid on the propulsor. Within each cycle (e.g., $3.0 \le t^* < 4.0$), the force profile consists of a region of positive force — over approximately the first half of the cycle, when the leading edge of the propulsor is moving in the negative z-direction

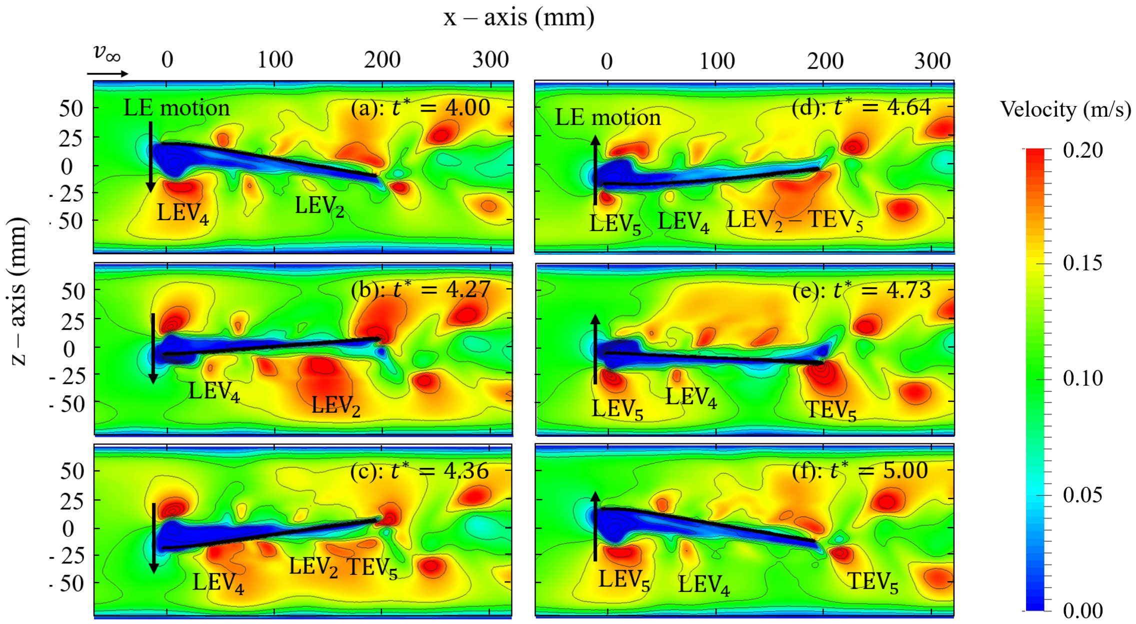

Fig. 13. Snapshots of velocity magnitude on the middle plane (i.e. 50%H), showing the leading edge vortices (LEVs) and trailing edge vortices (TEVs).

— followed by a region of negative force over roughly the second half of the cycle, when the leading edge is moving in the positive z-direction. As expected, once periodicity is reached, the two regions have the same shape, and opposite signs.

It is notable that each region of positive or negative force exhibits two peaks where the magnitude of force reaches a local maximum. This behavior stands in sharp contrast with the periodic flapping or heaving motion of *rigid* structures (e.g., rigid airfoils and hydrofoils), which generates only one peak in each "stroke". For better understanding, we plot the lengthwise distribution of hydrodynamic lateral force at four time instances between $t^* = 0.5$ and $t^* = 1.0$ (Figure 14(b)), together with the position of the propulsor midline (Figure 14(c)). At $t^* = 0.60$, the distributed lateral force is negative throughout the entire length of the propulsor, causing the total lateral force at that instance to be negative (Figure 14(b), (i)). This is the time when the first peak (−1.0 N) is reached, which is also the primary one. For $0.60 < t^* < 0.86$, the leading edge of the propulsor is moving in the positive z-direction, whereas the trailing edge is moving in the negative z-direction (Figure 14(c)). The difference in the direction of acceleration causes the lateral force to act in opposite directions. Specifically, at $t^* = 0.70$, the distributed lateral force is negative from the leading edge to approximately 75%L, and positive afterwards (Figure 14(b), (ii)). Due to the presence of distributed lateral force in opposite directions, the total lateral force is observed to decrease towards a local minimum (in terms of force magnitude) at point (iii) (Figure 14(a)). Point (iii) is at $t^* = 0.73$, which is close to the time when the leading edge is at its maximum velocity, but zero acceleration ($t^* = 0.75$). At $t^* = 0.86$, the distributed lateral force is positive from the leading edge to 18%L, then turns negative. This leads to a second peak total lateral force of −0.55 N.

Overall, it is evident that the appearance of two peaks results from the elasticity of the structure, which leads to nonlinear lengthwise variations in displacement, velocity, and acceleration. In addition, this phenomenon may also be related to dynamic stall and LEVs: owing to the flexibility of the fin, the angle of attack of the propulsor varies rapidly, causing strong LEV shedding, which briefly increases the lateral force before interacting with trailing edge vortices. Lastly, comparing the force distributions at (i) and (iv), it is noteworthy that the first peak is primarily due to the negative distributed lateral force occurring from the leading edge to approximately 50%L, while the second peak is primarily due to that from approximately 50%L to the trailing edge. This is also consistent with the structural motion and deformation presented in Figure 14(c), which shows that the first peak is reached when the leading edge is approximately at the maximum displacement, minimum velocity, and maximum acceleration; while the second peak

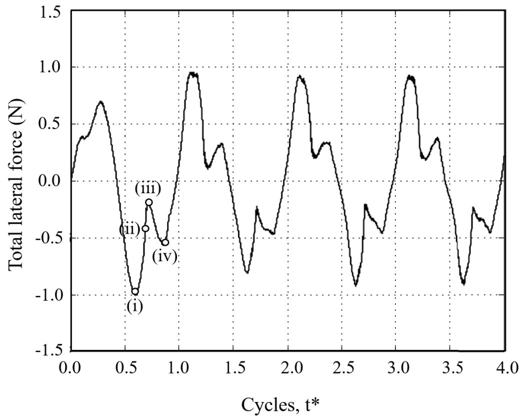

(a) Total lateral force

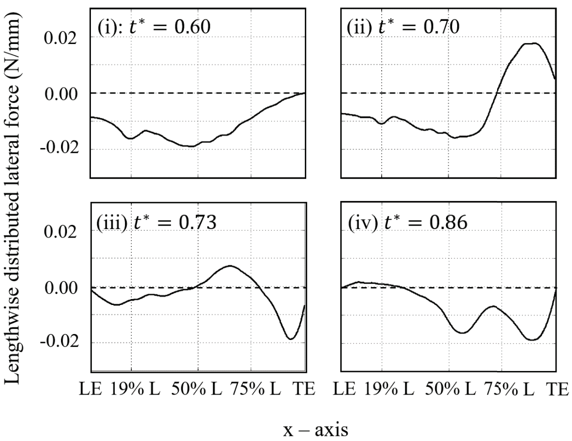

(b) Distribution of lateral force along propulsor length.

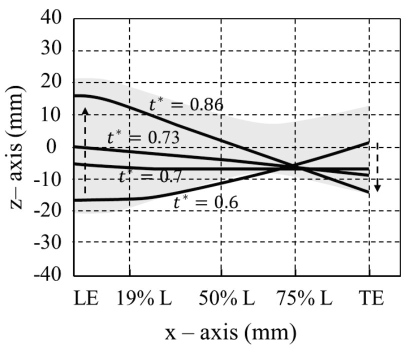

(c) Mid-width propulsor displacement

Fig. 14. Lateral hydrodynamic force. (LE: leading edge, TE: trailing edge)

is reached when the trailing is near such condition.

5.3. *Effect of propulsor shape: trapezoidal fin versus forked fin*

Different species of fish often have different shapes of caudal fin depending on their primary functions and abilities to swim and maneuver [37]. For instance, the so-called *sit-and-wait predators* typically have a wide caudal fin with large surface area (e.g., sculpin, flounder)[38]. They often stay still but need to maneuver with high acceleration to ambush on preys. On the contrary, *rover-predators* often use a caudal fin with small surface area (e.g., tuna, mackerel). They need to swim with constant speed over medium to long distances. In previous sections, we have studied a fin-and-joint propulsor with an artificial caudal fin of trapezoidal shape, which has relatively large surface area. Here, we introduce another, "forked" fin which has the same primary dimensions, yet much smaller surface area (Figure 15). Specifically, the modified propulsor has the same joint (i.e. the artificial caudal peduncle), and the fork starts at $45\%L$. The modified propulsor has a surface area of $6,300$ mm^2, in contrast with $12,600$ mm^2 for the original one. The joint of the modified propulsor is discretized using 336 nodes and 300 quadrangle elements, while the fin is discretized using $1,589$ nodes and $1,408$ quadrangle elements. The same material properties for polycarbonate (Table 1) are used for the modified propulsor. The setting of the fluid subsystem and the prescribed leading edge motion are also left unchanged.

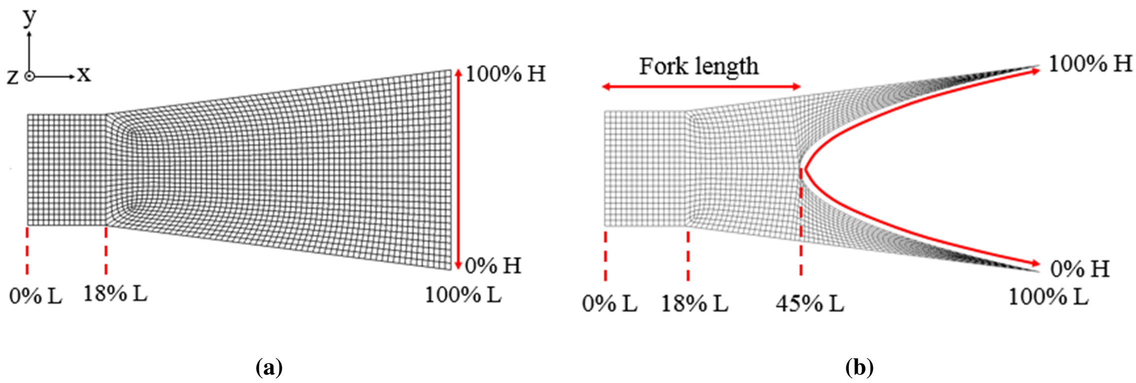

Fig. 15. Geometry and CSD mesh of two fin-and-joint propulsors with (a) a trapezoidal fin and (b) a forked fin.

Figure 16 compares the predicted structural motion and deformation between the two different propulsors. A phase lag along the length of the fin can be seen in both cases, because of the elasticity of the propulsor. Nonetheless, there is a dramatic difference in the displacement profile. The original propulsor with a trapezoidal fin shows a virtual pivot at approximately 2/3 of the length, where the displacement is much smaller than the prescribed leading edge displacement (5 mm versus 20 mm). On the other hand, the modified propulsor with a forked fin does not exhibit the same feature. Everywhere along the length of the propulsor, the temporal maximum displacement is either close to the prescribed leading edge displacement, or larger. Moreover, the temporal maximum displacement at the trailing edge differs between 13.7 mm for the trapezoidal fin and 28.1 mm for the forked fin. The larger displacement achieved by the propulsor with the forked fin can be related to the smaller surface area, which reduces the added mass effect.

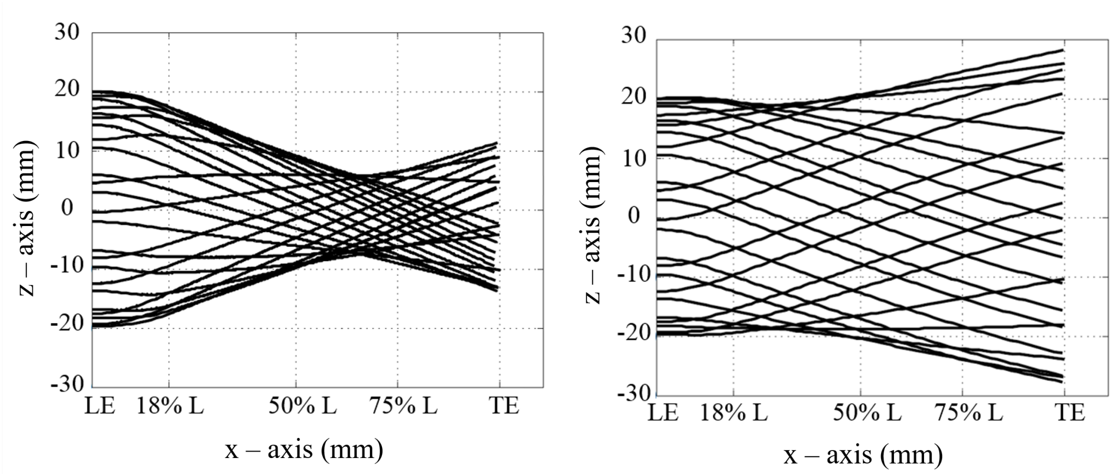

(a) Propulsor with a trapezoidal fin **(b)** Propulsor with a forked fin

Fig. 16. Top view of structural displacement for (a) the original propulsor with a trapezoidal fin and (b) the modified propulsor with a forked fin. In each sub-figure, 25 snapshots taken at a frequency of 12.5 Hz are superposed. (LE: leading edge, TE: trailing edge)

The time-averaged hydrodynamic thrust generated by the forked fin is significantly higher than that by the trapezoidal fin. For fin thickness $\tau = 1.6$ mm, the former is found to be 0.0165 N, whereas the latter, as reported in Figure 5, is -0.00047 N (drag). To investigate the difference, we again visualize the time-averaged flow velocity on two x-z planes interacting the mid-width (50%H) and the edge (95%H) of the modified propulsor (Figure 17), which can be compared against results for the original propulsor, shown in Figure 12. Also, the time-averaged flow velocity at 22%L aft of the trailing edge is plotted separately (Figures 17(c) and 17(d)).

Figure 17(a) clearly shows a momentum surfeit wake at 50%H, i.e. $v/v_\infty > 1.0$, which indicates thrust production. This general behavior is similar to that observed on the original propulsor with a trapezoidal fin (Figure 12(a)). Nonetheless, at 22%L aft of the trailing edge, the maximum time-averaged velocity is $v = 2.5v_\infty$ (Figure 17(c)), whereas that for the original propulsor is significantly lower, approximately $v = 1.5v_\infty$ (Figure 12(c)). At the x-z plane intersecting 95%H (Figure 17(b)), a momentum deficit wake is still evident, qualitatively similar to that observed for the original propulsor (Figure 12(b)). However, at 22%L aft of the trailing edge, the minimum time-averaged velocity is $v = 0.9v_\infty$ (Figure 17(d)), which is higher than that for the original propulsor, $v = 0.6v_\infty$ (Fig. 12(d)). This comparison suggests that the increase in total thrust obtained by the forked fin is like a result of both an enhanced thrust production around the mid-plane, and a drag reduction around the two edges. It is also worth mentioning that the higher time-averaged thrust for the forked fin is consistent with findings in biology, specifically, that fish with a narrow, forked caudal fin often like (and need) to cruise for long distances.

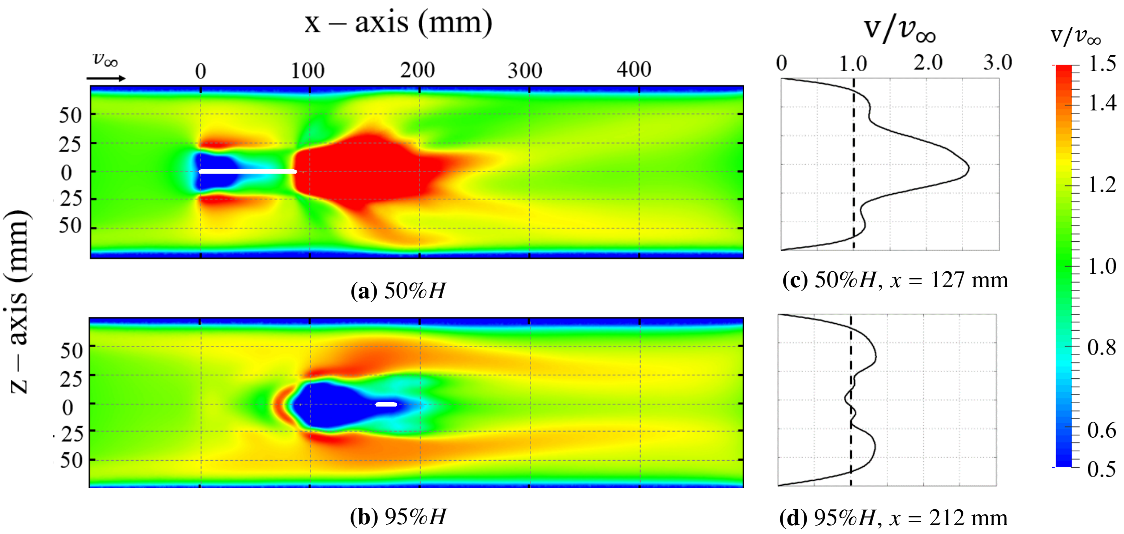

Fig. 17. Modified propulsor with a forked fin: Time-averaged velocity field on two x-z planes intersecting (a) 50%H and (b) 95%H, and along the line at 22%L aft of trailing edge.

Figure 18 compares the time-history of total lateral force generated by the two propulsors. The force profile of the modified propulsor still have two peaks over each stroke of prescribed leading edge motion, same as the original propulsor. Nonetheless, the magnitude of lateral force is much lower. In particular, the maximum peak-to-peak lateral force for the modified propulsor is 1.95 N, whereas that for the original one is 1.14 N, in other words, 41.5% lower. This observation also agrees with biological findings, particularly that fish with a wide caudal fin often have superior abilities to maneuver with high acceleration [39].

6. Concluding remarks

In aerospace and ocean engineering, fluid-structure interaction has been considered primarily as an undesirable phenomenon, associated with flutter, buffeting, and other problems that must be mitigated or avoided in design and operation. Nonetheless, studies of aerial and aquatic animals have indicated the possibility of taking advantage of fluid-structure interaction to achieve both propulsion efficiency and versatility, which may be particularly suitable to small-scale, unmanned vehicles. Despite the promise, however, the introduction of additional variables (e.g., elasticity and viscoelasticity properties, actuations) and more complex physics (e.g., large deformation, unsteady flow) makes designing such propulsion systems a formidable challenge. In a broad sense, the present work attempts to explore

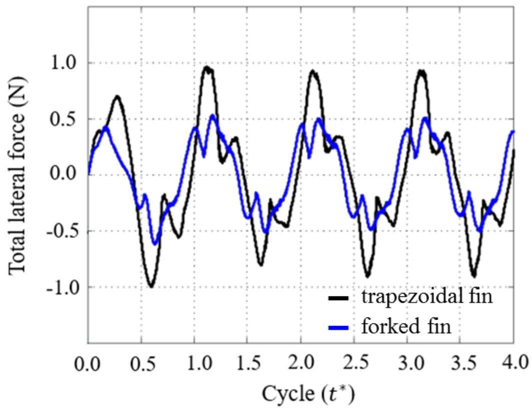

Fig. 18. Time-history of total lateral hydrodynamic force: Comparison between the modified propulsor with a forked fin and the original propulsor with a trapezoidal fin.

the possibility of coupling high-fidelity computational fluid and structural dynamics methods to *predictively* simulate flexible, biomimetic propulsors, and beyond this point, to quantitatively assess detailed design options.

Specifically, we apply a novel CFD-CSD coupled computational framework, referred to as "FIVER", to simulate the underwater flapping propulsion of a fin-and-joint system, which serves as a simplified engineering model of tail-dominated fish propulsion. This problem entails several challenges, including 3D unsteady fluid flow, large structural motion and deformation, and strong added-mass effect. We handle these issues using 3D CFD and CSD models, an embedded boundary method, the ANDES nonlinear shell model, and a numerically-stable partitioned fluid-structure coupling procedure.

We start with validating the CFD and CSD models using data — specifically, hydrodynamic forces, fundamental vibration frequency, and full-field displacement — obtained from modal testing and water tunnel experiments. In all the cases, the numerical results agree reasonably well with the experimental data. Next, we investigate the coupled fluid and structural dynamics, as well as the propulsive performance, using the simulation result. In this regard, previous numerical analyses on flexible propulsors are often limited to one-way coupling and/or two-dimension. We focus on the two-way interaction between the fluid and the propulsor, as well as the flow variation in 3D. A few findings are noteworthy. First, due to the elasticity of the structure and the strong added-mass effect, the structural kinematics is nonlinear lengthwise. This leads to several interesting, and related phenomena, including a phase lag between the leading edge and the trailing edge of the propulsor, the occurrence of two peaks in the lateral force profile, and the generation and interaction of leading edge vortices and trailing edge vortices. Second, the fluid dynamics varies significantly along the width of the propulsor. Instantaneous flow snapshots show the presence of a reverse von Kármán street on the mid-width plane, which gradually transforms to a von Kármán street near the two edges. Both the instantaneous and the time-averaged flow suggest, for the propulsor with a trapezoidal fin, that the mid-plane region tends to produce thrust, whereas the regions near the two edges tend to produce drag.

Further, motivated by the diversity in fish locomotion, we modify the original, trapezoidal fin to obtain a "forked" fin with a 50% smaller surface area. The fluid and structural dynamics and the hydrodynamic forces of the two propulsors are compared and contrasted. In all these aspects, the effect of fin geometry is significant. In particular, we find that the forked fin generates larger thrust, yet smaller lateral force compared to the trapezoidal fin. This result is consistent with findings in biology, particularly that fish with a narrow, forked caudal fin often cruise for long distances, while those with a wide caudal fin tend to have superior abilities to maneuver with high acceleration.

Finally, it is worth mentioning that despite two fin shapes, many other variables, such as the propulsor dimensions, the free-stream flow velocity, and the parameters of the actuation function, have been fixed throughout this work. Therefore, applying the findings of this study to other scenarios should be done with caution. Also, we have applied our compressible Navier-Stokes CFD solver, equipped with a low-Mach preconditioner, to simulate a hydroelasticity problem in which the fluid flow can be considered incompressible. It may be possible to solve the problem more efficiently using an incompressible CFD solver. Nonetheless, this is beyond the scope of our current study.

Acknowledgements

The authors gratefully acknowledge the financial support of the National Science Foundation (NSF) under Award Numbers CBET-1751487 and EFRI-0938043, an Air Force Summer Faculty Fellowship offered to K.G.W., and the faculty start-up support from Virginia Tech to K.G.W. The authors also thank Dr. Ashok K. Kancharala for his valuable assistance with model development and calibration.

Appendix A. Water tunnel fin-and-joint propulsion experiments

Experiments have been performed to evaluate the effect of caudal fin and caudal peduncle stiffness on propulsive performance ([13, 14]). Specifically, trapezoidal foils mimicking the caudal fin of fish are fabricated from polycarbonate (PC) sheets, with the same length and width, but different thickness (τ) values ranging from 0.2 to 3.2 mm. Rectangular foil of 0.4 mm thick PC sheets have been used to mimic the caudal peduncle of the fish, referred to as the *joint*. The joint and the fins are attached together using a small aluminum plate. The dimensions of this biomimetic fin-and-joint system are provided in Figure 1.

The fabricated fin-and-joint specimens are tested in a recirculating water tunnel with dimensions of 457.2 mm $\times$ 152.4 mm $\times$ 152.4 mm (18 in $\times$ 6 in $\times$ 6 in). The experimental setup is shown in Figure A.19. A constant freestream flow velocity v_∞ = 0.1 m/s is maintained throughout the experiments. A CUI M223X0003 brushed direct current (DC) motor attached with encoders is used to generate the heaving motion. A six-axis force transducer, ATI MINI40, measures the hydrodynamic forces and moments acting on the specimen. Along with the force measurement, digital image correlation (DIC) is used to capture the kinematics of the specimens heaving under water. Specifically, DIC tracks the speckles on the specimen (see Figure 1(b)) using digital image processing methods to calculate the 3D displacements. The DIC cameras capture the images at a frequency of 12 Hz. The LabView 2011 software is used to run the motors and collect the encoder and force data using a DAQ6211. Additional details on the experimental setup and data collection can be found in [13].

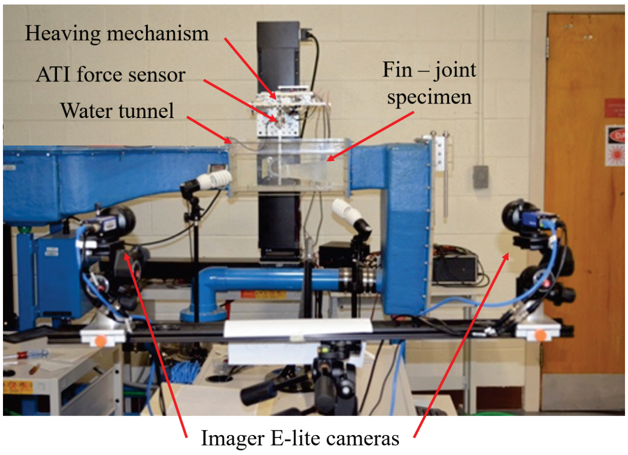

Fig. A.19. Experimental setup for evaluating the artificial fins in the water tunnel

References

[1] C. C. Eriksen, T. J. Osse, R. D. Light, T. Wen, T. W. Lehman, P. L. Sabin, J. W. Ballard, A. M. Chiodi, Seaglider: A long-range autonomous underwater vehicle for oceanographic research, IEEE Journal of Oceanic Engineering 26 (4) (2001) 424–436.

[2] D. Bingham, T. Drake, A. Hill, R. Lott, The application of autonomous underwater vehicle (auv) technology in the oil industry–vision and experiences, in: Fig XXII International Congress, 2002, pp. 19–26.

[3] G. Li, Y. Deng, O. L. Osen, S. Bi, H. Zhang, A bio-inspired swimming robot for marine aquaculture applications: From concept-design to simulation, in: OCEANS 2016-Shanghai, IEEE, 2016, pp. 1–7.

[4] R. W. Button, J. Kamp, T. B. Curtin, J. Dryden, A survey of missions for unmanned undersea vehicles, Tech. rep., RAND Corporation, Santa Monica, CA (2009).
[5] T. Y. Wu, Fish swimming and bird/insect flight, Annual Review of Fluid Mechanics 43 (2011) 25–58.
[6] G. V. Lauder, Fish locomotion: Recent advances and new directions, Annual Review of Marine Science 7 (2015) 521–545.
[7] A. J. Ijspeert, Biorobotics: Using robots to emulate and investigate agile locomotion, Science 346 (6206) (2014) 196–203.
[8] R. Pfeifer, M. Lungarella, F. Iida, The challenges ahead for bio-inspired 'soft' robotics, Communications of the ACM 55 (11) (2012) 76–87.
[9] C. J. Esposito, J. L. Tangorra, B. E. Flammang, G. V. Lauder, A robotic fish caudal fin: Effects of stiffness and motor program on locomotor performance, Journal of Experimental Biology 215 (1) (2012) 56–67.
[10] J. L. Tangorra, G. V. Lauder, I. W. Hunter, R. Mittal, P. G. Madden, M. Bozkurttas, The effect of fin ray flexural rigidity on the propulsive forces generated by a biorobotic fish pectoral fin, Journal of Experimental Biology 213 (23) (2010) 4043–4054.
[11] G. V. Lauder, B. Flammang, S. Alben, Passive robotic models of propulsion by the bodies and caudal fins of fish, Integrative and Comparative Biology 52 (5) (2012) 576–587.
[12] M. Sfakiotakis, D. M. Lane, J. B. C. Davies, Review of fish swimming modes for aquatic locomotion, IEEE Journal of Oceanic Engineering 24 (2) (1999) 237–252.
[13] A. Kancharala, M. Philen, Study of flexible fin and compliant joint stiffness on propulsive performance: Theory and experiments, Bioinspiration & Biomimetics 9 (3) (2014) 036011.
[14] A. Kancharala, M. Philen, Enhanced hydrodynamic performance of flexible fins using macro fiber composite actuators, Smart Materials and Structures 23 (11) (2014) 115012.
[15] C. Farhat, A. Rallu, K. Wang, T. Belytschko, Robust and provably second-order explicit–explicit and implicit–explicit staggered time-integrators for highly non-linear compressible fluid–structure interaction problems, International Journal for Numerical Methods in Engineering 84 (1) (2010) 73–107.
[16] K. Wang, A. Rallu, J.-F. Gerbeau, C. Farhat, Algorithms for interface treatment and load computation in embedded boundary methods for fluid and fluid–structure interaction problems, International Journal for Numerical Methods in Fluids 67 (9) (2011) 1175–1206.
[17] C. Farhat, V. K. Lakshminarayan, An ALE formulation of embedded boundary methods for tracking boundary layers in turbulent fluid–structure interaction problems, Journal of Computational Physics 263 (2014) 53–70.
[18] E. Turkel, Preconditioned methods for solving the incompressible and low speed compressible equations, Journal of Computational Physics 72 (2) (1987) 277–298.
[19] C. Militello, C. A. Felippa, The first ANDES elements: 9-dof plate bending triangles, Computer Methods in Applied Mechanics and Engineering 93 (2) (1991) 217–246.
[20] K. Wang, J. Grétarsson, A. Main, C. Farhat, Computational algorithms for tracking dynamic fluid–structure interfaces in embedded boundary methods, International Journal for Numerical Methods in Fluids 70 (4) (2012) 515–535.
[21] C. Farhat, A. Larat, A. Main, P. Avery, K. Wang, C. Saint-Jalm, An embedded boundary method for viscous fluid/structure interaction problems and application to flexible flapping wings, in: 42nd AIAA Fluid Dynamics Conference and Exhibit, AIAA 2012–2688, 2012.
[22] V. K. Lakshminarayan, C. Farhat, Nonlinear aeroelastic analysis of highly flexible flapping wings using an ALE formulation of embedded boundary method, in: AIAA Science and Technology Forum and Exposition, AIAA 2014-0221, 2014.
[23] C. S. Peskin, The immersed boundary method, Acta Numerica 11 (2002) 479–517.
[24] R. Glowinski, T.-W. Pan, A. J. Kearsley, J. Periaux, Numerical simulation and optimal shape for viscous flow by a fictitious domain method, International Journal for Numerical Methods in Fluids 20 (8-9) (1995) 695–711.
[25] I. Borazjani, L. Ge, T. Le, F. Sotiropoulos, A parallel overset-curvilinear-immersed boundary framework for simulating complex 3D incompressible flows, Computers & Fluids 77 (2013) 76–96.
[26] H. Dong, M. Bozkurttas, R. Mittal, P. Madden, G. Lauder, Computational modelling and analysis of the hydrodynamics of a highly deformable fish pectoral fin, Journal of Fluid Mechanics 645 (2010) 345–373.
[27] M. S. U. Khalid, I. Akhtar, H. Dong, Hydrodynamics of a tandem fish school with asynchronous undulation of individuals, Journal of Fluids and Structures 66 (2016) 19–35.
[28] R. Bottom II, I. Borazjani, E. Blevins, G. Lauder, Hydrodynamics of swimming in stingrays: Numerical simulations and the role of the leading-edge vortex, Journal of Fluid Mechanics 788 (2016) 407–443.
[29] C. Farhat, J.-F. Gerbeau, A. Rallu, Fiver: A finite volume method based on exact two-phase riemann problems and sparse grids for multi-material flows with large density jumps, Journal of Computational Physics 231 (19) (2012) 6360–6379.
[30] Y. Li, Equation of state of water and sea water, Journal of Geophysical Research 72 (10) (1967) 2665–2678.
[31] A. Main, X. Zeng, P. Avery, C. Farhat, An enhanced fiver method for multi-material flow problems with second-order convergence rate, Journal of Computational Physics 329 (2017) 141–172.
[32] V. Tech, Advanced Research Computing at Virginia Tech, https://secure.hosting.vt.edu/www.arc.vt.edu/computing/blueridge-sandy-bridge/ (August 2016).
[33] M. Géradin, D. J. Rixen, Mechanical vibrations: Theory and application to structural dynamics, John Wiley & Sons, 2014.
[34] N. Imamura, K. Matsuuchi, Relationship between vortex ring in tail fin wake and propulsive force, Experiments in Fluids 54 (10) (2013) 1605.
[35] P. Linden, J. Turner, 'Optimal' vortex rings and aquatic propulsion mechanisms, Proceedings of the Royal Society of London B: Biological Sciences 271 (1539) (2004) 647–653.
[36] H. R. Vallentine, Applied hydrodynamics, Springer, 2013.
[37] K. L. Feilich, G. V. Lauder, Passive mechanical models of fish caudal fins: Effects of shape and stiffness on self-propulsion, Bioinspiration & Biomimetics 10 (3) (2015) 036002.
[38] R. W. Blake, Fish functional design and swimming performance, Journal of Fish Biology 65 (5) (2004) 1193–1222.
[39] P. Webb, G. Smith, Function of the caudal fin in early fishes, Copeia 1980 (3) (1980) 559–562.